Heliyon 8 (2022) e09555

Contents lists available at ScienceDirect

Heliyon

journal homepage: www.cell.com/heliyon

Research article

Structural characterization of the water-soluble porphyrin complexes $[Fe^{II}(TPPS)\ (NO^{\bullet})]^{4-}$ and $[\mu\text{-O-}([Fe^{III}(TPPS)])_2]^{8-}$

Agostina Mazzeo [a], Carina Gaviglio [b], Juan Pellegrino [a,**], Fabio Doctorovich [a,*]

[a] Departamento de Química Inorgánica, Analítica, y Química Física, Facultad de Ciencias Exactas y Naturales, Universidad de Buenos Aires, INQUIMAE-CONICET, Ciudad Universitaria, Pab. 2, C1428EHA, Buenos Aires, Argentina

[b] Departamento de Física de la Materia Condensada, Gerencia Física (CAC), Gerencia de Area de Investigaciones y Aplicaciones no nucleares, Comisión Nacional de Energía Atómica, Avenida General Paz 1499, San Martín, Buenos Aires, Argentina

HIGHLIGHTS

- The crystal structure of biomimetic complex $[Fe^{II}(TPPS)\ (NO^{\bullet})]^{4-}$ is presented.
- Ferric oxodimer $[\mu\text{-O-}([Fe^{III}(TPPS)])_2]^{8-}$ is also structurally characterized.
- Both structures are described and compared to those of related complexes.

ARTICLE INFO

Keywords:
Iron porphyrin
Iron nitrosyl
Water-soluble
Coordination complex
Crystal structure

ABSTRACT

Iron water-soluble porphyrins have been long used as biomimetic compounds for modelling the active sites found in heme-enzymes. In this regard, the anionic porphyrin $[Fe^{III}(TPPS)]^{3-}$ and its coordination complexes have been repeatedly chosen as suitable water-soluble platforms for bioinorganic chemistry studies. In this work we report for the first time the crystal structure of the water-soluble nitrosyl complex $[Fe^{II}(TPPS)\ (NO^{\bullet})]^{4-}$ along with that of oxodimeric ferric species $[\mu\text{-O-}([Fe^{III}(TPPS)])_2]^{8-}$.

1. Introduction

X-ray diffraction is clearly one of the most powerful characterization techniques, and bioinorganic chemists are eager to take advantage of it to study their model compounds whenever it is possible. The structural characterization of these compounds enables interesting comparisons with their biological counterparts, regarding both the "active site" and the second coordination sphere. In this context, the study of metalloporphyrin complexes acting as heme-enzyme models becomes a relevant matter, and therefore, many crystal structures have been reported, obtained mainly in organic media. In particular, the structures of many *meso*-tetraarylporphyrins have been extensively studied, displaying an interesting array of intermolecular channels and cavities that can accommodate a wide variety of molecular guests [1].

Regarding the structural elucidation of porphyrin complexes with nitric oxide and related species, which are relevant as biomimetic models for heme-enzyme intermediates of the nitrogen cycle [2], the fundamental work of Dr. Scheidt and coworkers comprises the most complete and detailed guide, including $\{MNO\}^{6,7,8}$ complexes – according to the Enemark-Feltham notation [3] – with M = Fe, Mn and Co [4]. Throughout their studies, intrinsic structural disorder was found in the MNO fragments, which avoids the exact determination of certain key parameters such as M-NO and N-O distances and the M-N-O angle. However, the structural elucidation of these species remains of central importance for determining expected variations, for example, along different oxidation states of the MNO entity, or arising from modifications in the heme platform, which helps to establish analogies with the biological systems they intend to model. Interestingly, even the crystal structures of highly unstable $\{FeNO\}^8$ porphyrin complexes $[K(2.2.2)][Fe^{II}(OEP)\ (NO^{-})]$ and $[Co(Cp)_2][Fe^{II}(TFPPBr_8)\ (NO^{-})]^{-}$ could be determined in the last few years [5, 6], contributing to the understanding of these reduced systems which could resemble reactive intermediates in catalytic mechanisms in enzymes of the nitrogen cycle, such as nitric oxide and nitrite reductases [7].

* Corresponding author.
** Corresponding author.
E-mail addresses: pellegrino@qi.fcen.uba.ar (J. Pellegrino), doctorovich@qi.fcen.uba.ar (F. Doctorovich).

https://doi.org/10.1016/j.heliyon.2022.e09555
Received 4 April 2022; Received in revised form 10 May 2022; Accepted 25 May 2022

All reported examples of iron nitrosyl porphyrin complexes were obtained in organic media. In fact, very few crystalline structures of water-soluble metalloporphyrins have been reported at all, including diaquo Ir(III) and Co(III) complexes of anionic $TPPS^{4-}$ [8, 9], and both the monomeric and oxodimeric species of ferric $[Fe^{III}(TMPyP)]^{5+}$ [10, 11]. In most cases, both the obtention of crystalline material and the application of appropriate data refining algorithms resulted considerably more challenging than in organic media. The structural elucidation of water-soluble FeNO porphyrin complexes, in this context, arises as an interesting research goal, which aims to make relevant comparisons with organosoluble analogues and, hopefully, pointing out the influence of solvent effects.

In most works about $\{FeNO\}^7$ porphyrin complexes, these species are generated *in situ* via Fe(III) chemical reduction (for example, with sodium dithionite) followed by $NO^{\bullet}$ (g) bubbling, or directly via reductive nitrosylation when possible [12, 13]. The presence of trace impurities is almost inevitable, especially when working in an aqueous environment. In this work, we have taken advantage of the previously reported isolation method for $Na_4[Fe^{II}(TPPS)\ (NO^{\bullet})]$ from the reaction of $Na_3[Fe^{III}(TPPS)]$ and the HNO donor 4-nitro Piloty's acid (4-NO_2-PA) [14], which allows a more careful purification, to obtain the first crystalline sample of a water soluble $\{FeNO\}^7$ porphyrin complex. We have also successfully obtained the first crystal structure of ferric precursor $[Fe^{III}(TPPS)]^{3-}$ as the oxodimeric species. The structures of both complexes are shown in Figure 1.

2. Results and discussion

2.1. $(BTMA)_2Mg[Fe^{II}(TPPS)\ (NO^{\bullet})]$

Although thin crystals could be prepared from the sodium salt $Na_4[Fe^{II}(TPPS)\ (NO^{\bullet})]$, most of them either did not diffract, or collapsed when placed in loop oil, and so ion-exchange procedures were carried out. Only when the counterion was exchanged for benzyltrimethylammonium ($BTMA^+$), as described in the Experimental Section, good quality crystals could be obtained. Bis(triphenylphosphine)iminium was also evaluated as an alternative although its salts did not yield suitable crystals.

Crystals were obtained after several weeks via slow acetone diffusion into saturated aqueous solutions of the nitrosyl complex under argon atmosphere, as detailed in the Experimental Section. Low temperature (100K) measurements were required to obtain suitable data.

There are two molecules per unit cell, as shown in Figure 2, with the NO ligand pointing in opposite directions. The complex is pentacoordinate, as there is no water molecule occupying the vacant axial position; this illustrates the *trans*-labilization effect exhorted by the $NO^{\bullet}$ ligand [15]. As the structure was solved, hexaaquamagnesium(II) cations were also identified (Figure 2, left), likely arising from the nitrosylation step, which involves an HNO donor that is synthesized in the presence of excess MgO. Two $BTMA^+$ cations per asymmetric unit are also observed, compensating the 4- charge of the anionic complex. The cations are oriented near the negatively charged 4-sulfonate substituents.

A lateral view of a single porphyrin complex with and without solvent molecules and counterions can be seen in Figure 3. It can be observed that the 4-sulfonatophenyl *meso* substituents appear almost perpendicular to the porphyrin ring. Relevant crystallographic information and selected structural parameters are shown in Table 1.

The porphyrin core of $[Fe^{II}(TPPS)\ (NO^{\bullet})]^{4-}$, devoid of the *meso* substituents, is shown in Figure 4. The structure displays a saddled conformation, with atoms positioned above and below the porphyrin 24-atom mean plane, which is shown in pink in Figure 4 (left). The individual atomic displacements from the mean plane, measured in angstroms, are shown in Figure 4 (right); atoms below the mean plane are more lightly colored. It can be observed that the four pyrrolic rings appear alternatively above and below the porphyrin mean plane, while *meso* carbon atoms remain essentially coplanar. This saddled conformation has also been observed in many M(TPP)L (TPP: tetra-*meso*-tetraphenyl porphyrinate) pentacoordinate complexes, probably due to the presence of bulky phenyl substituents [16]. On the other hand, in β substituted porphyrins, the core ring can remain virtually flat [5]. Different non-planar distortions of porphyrin rings have also been observed in many hemeproteins and appear to play a key role in their specific functions [17].

The structure is generally well resolved, although as usual, there is significant disorder in the NO fragment, as evidenced by the disproportionally large probability ellipsoids [18]. Two orientations of such fragment are simultaneously observed, and both of them involve large N-O distances, which is characteristic of suboptimal quality data. As Scheidt and coworkers stated [4], the N-O distance is expected to

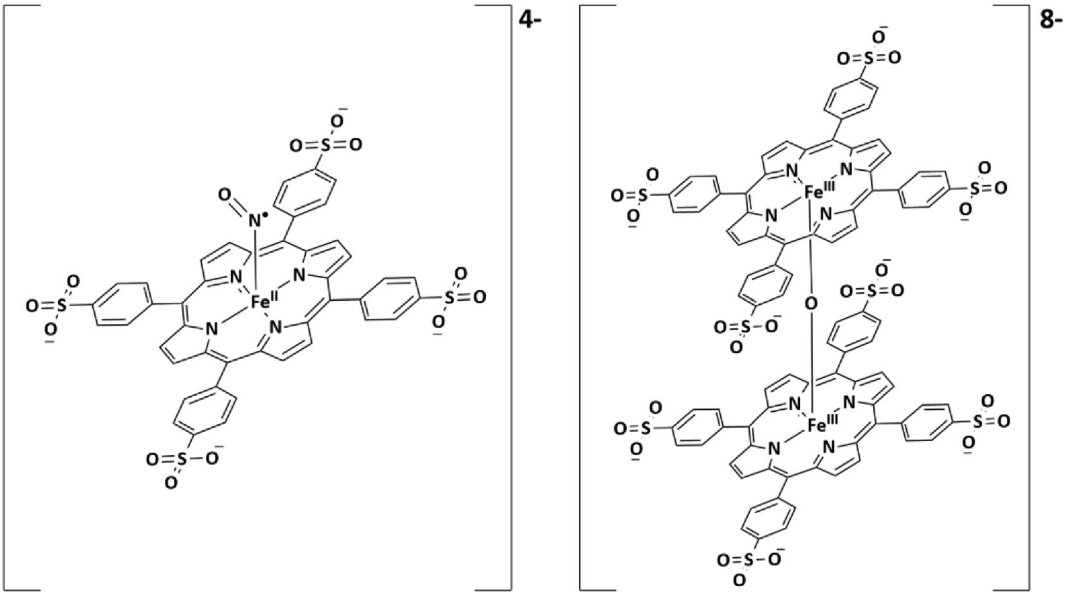

Figure 1. Chemical structures of anionic complexes $[Fe^{II}(TPPS)\ (NO^{\bullet})]^{4-}$ (left) and $[\mu\text{-O-}([Fe^{III}(TPPS)])_2]^{8-}$ (right).

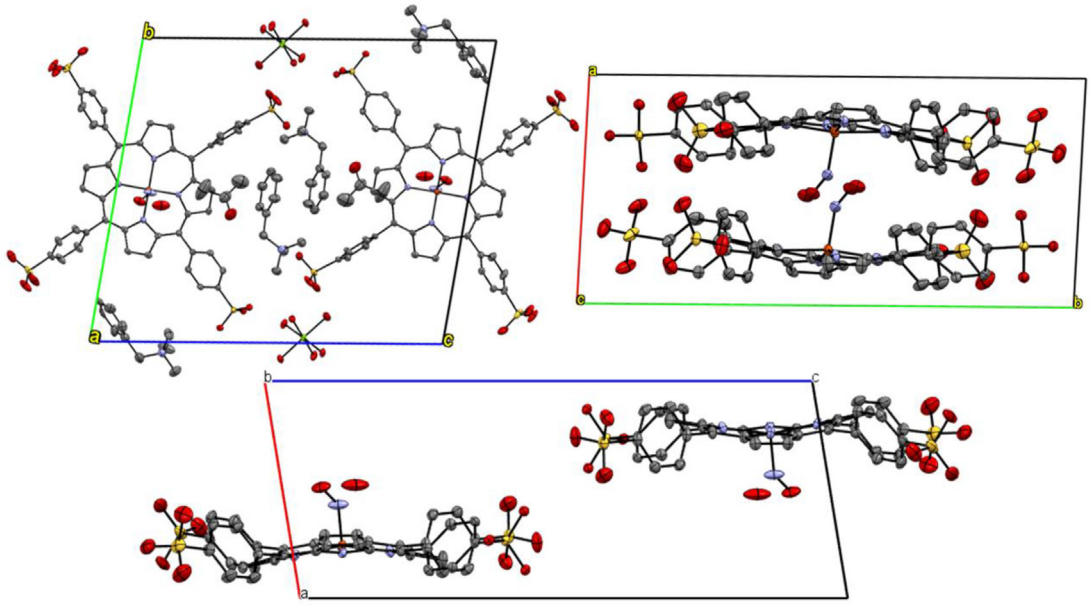

Figure 2. ORTEP plot of $(BTMA)_2Mg[Fe^{II}(TPPS)(NO^{\bullet})]$ at the 50% probability level showing the crystal packing and unit cell along its three axes. $BTMA^{+}$ and $[Mg(H_2O)_6]^{2+}$ cations as well as nearby acetone molecules are only shown in the top left view for clarity reasons. Hydrogen atoms were omitted for clarity.

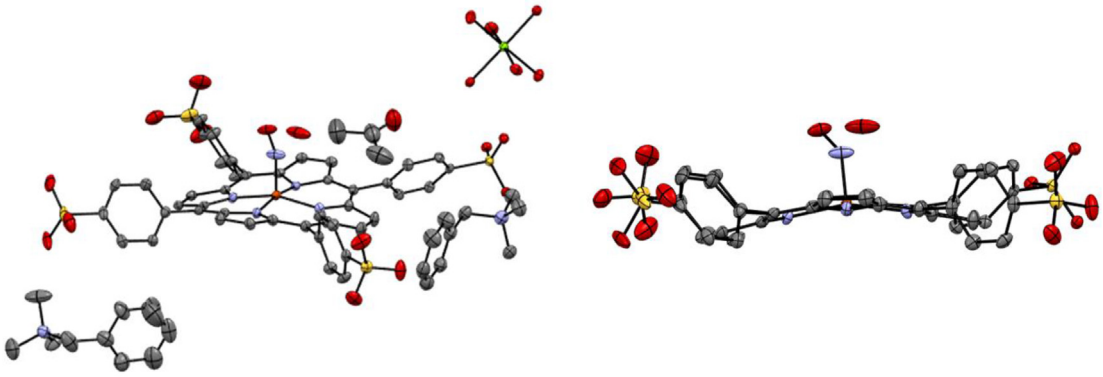

Figure 3. ORTEP plots of $(BTMA)_2Mg[Fe^{II}(TPPS)(NO^{\bullet})]$ at the 50% probability level. Left: showing $BTMA^{+}$ and $[Mg(H_2O)_6]^{2+}$ counterions and a nearby acetone molecule. Right: lateral view of porphyrin complex. Hydrogen atoms were omitted for clarity.

remain essentially unchanged from that found in free nitric oxide (1.15 Å) which is not the case as shown in Figure 5. The more disordered O atom (as depicted by the larger ellipsoid) gives the longer N-O distance and the smaller Fe-N-O angle, both values being less similar to typical values found in $\{FeNO\}^7$ complexes as shown in Table 2. On the contrary, the N-O distance of 1.243 Å and Fe-N-O angle of 136.08° found in the remaining orientation are closer to reported values. Although smaller values for Fe-N-O angles have been reported, as seen in Table 2, elongated N-O distances were also observed in these cases [19].

From a top perspective, the $NO^{\bullet}$ ligand is oriented between two Fe-N_{PORF} bonds, with the smallest O-N-Fe-N_{PORF} dihedral angle having a value of 41.46°. The iron atom is 0.247 Å out of the porphyrin plane, in accordance with reported values. The Fe-NO vector is tilted 7.8° from the porphyrin mean plane normal, representing a horizontal displacement of 0.234 Å between the N(NO) atom and the iron atom.

As in previously reported cases, the four Fe-N_{PORF} distances are not equal, and can be grouped in two pairs of similar values, in this case, 1.982–1.987 Å and 1.999–2.003 Å. This asymmetry is a characteristic property of the molecular structure of pentacoordinate $\{FeNO\}^7$ porphyrin complexes, which does not seem to depend on the nature of the porphyrin ring or intermolecular interactions, and has also been observed in naturally occurring porphyrinates [18, 22]. This is related to the aforementioned tilting of the N-O vector, as previously described: the shorter Fe-N_{PORF} distances correspond to the side towards which the N-O vector is tilted.

Although no water molecules can be seen near the FeNO fragment in $[Fe^{II}(TPPS)(NO^{\bullet})]^{4-}$, two acetone molecules are observed interacting with the NO oxygen atom via hydrogen bonding interactions as shown in Figure 6. Distances between the O atom and H atoms from the nearest acetone molecule range between 2.22 and 3.33 Å. Notably, reports of direct interactions between the NO fragment of $\{FeNO\}^7$ complexes with solvent molecules are not frequently found in the literature [19].

2.2. $(BTMA)_8[\mu\text{-}O\text{-}(Fe^{III}(TPPS))_2]$

Even though the anionic iron porphyrin $[Fe^{III}(TPPS)]^{3-}$ has been widely explored as a catalyst in general [23] and as a water-soluble

Table 1. Crystallographic information and selected structural parameters for $(BTMA)_2Mg[Fe^{II}(TPPS)(NO^{\bullet})]$.

$(BTMA)_2Mg[Fe^{II}(TPPS)(NO^{\bullet})]$	
Crystallographic Information	
Space Group	P-1
Crystal System	Triclinic
a (Å)	9.1095 (4)
b (Å)	19.7734 (9)
c (Å)	22.9644 (10)
a (°)	79.838 (2)
β (°)	80.129 (2)
γ (°)	85.701 (2)
R_1	6.14
Selected distances and angles	
Fe-NO (Å)	1.718
Avg. N-O (Å)	1.272
Avg. Fe-N_{PORF} (Å)	1.993
ΔFe out of plane (Å)	0.247
Avg. Fe-N-O (°)	134
FeNO *tilting* (°)	7.83
N_{PORF}-Fe-N-O dihedral (°)	41.46

hemeprotein model in particular [24], no crystal structure of this complex could be found in literature. Attempts had been made at different pH values, but to no avail [10]. Taking advantage of the counterion-exchange protocol explored for $[Fe^{II}(TPPS)(NO^{\bullet})]^{4-}$, we focused on obtaining a crystalline sample of $(BTMA)_3[Fe^{III}(TPPS)]$, using the same crystallization method – acetone vapor diffusion – but this time on a methanolic saturated solution, given the lower water solubility of this complex. No special air-free techniques were employed in this experiment since the complex is not oxygen-sensitive.

After several weeks, needle-shaped metallic purple crystals were obtained, which could be analyzed via X-ray diffraction. In all cases, the obtained samples corresponded to the oxodimeric form; no monomeric samples could be prepared, even in the presence of acid.

Figure 7 shows the unit cell of $(BTMA)_8[\mu\text{-O-}(Fe^{III}(TPPS))_2]$, containing six dimeric units. For each dimer, only one $BTMA^+$ cation is explicitly visible; the remaining counterions presented considerable disorder to be modelled, and a solvent mask had to be applied using the

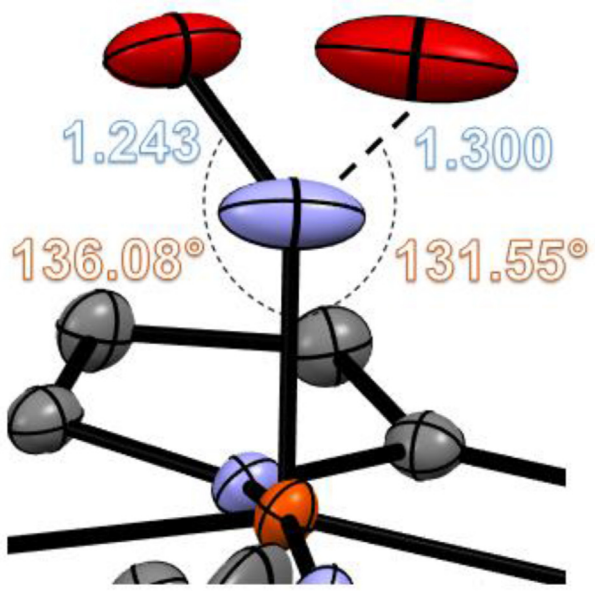

Figure 5. ORTEP plot of the FeNO fragment in $(BTMA)_2Mg[Fe^{II}(TPPS)(NO^{\bullet})]$ at the 50% probability level showing the two orientations of the NO ligand with their respective N-O distances and Fe-N-O angles.

Table 2. Characteristic structural parameters for selected $\{FeNO\}^7$ complexes.

Complex	Fe-N-O (°)	*Tilt* FeNO (°)	N-O (Å)	ΔFe (Å)[†]	Ref
$[Fe(TFPPBr_8)(NO^{\bullet})]$	148.5	5	1.131	0.36	[6]
[Fe(3,5-Me-BAFP) ($NO^{\bullet}$)]	146[a]	0.09	1.15	0.36[a]	[20]
[Fe(TPP) ($NO^{\bullet}$)]	144.5[b]	5.6	1.163	0.20[b]	[21]
[Fe(OEP) ($NO^{\bullet}$)]	143.5[a]	7	1.167	0.28[a]	[5]
[Fe(TTMP) ($NO^{\bullet}$)]	134.4[c]	3	1.236	0.25	[19]
$[Fe(TPPS)(NO^{\bullet})]^{4-}$	**134.2[c]**	**7.8**	**1.243**	**0.25**	this work
[Fe(TMP) ($NO^{\bullet}$)]	129.2[c]	0.5	1.293	0.32	[19]

[†]: Fe atom displacement from porphyrin mean plane. a: average of two structures b: measured at 33K. c: average of two NO orientations.

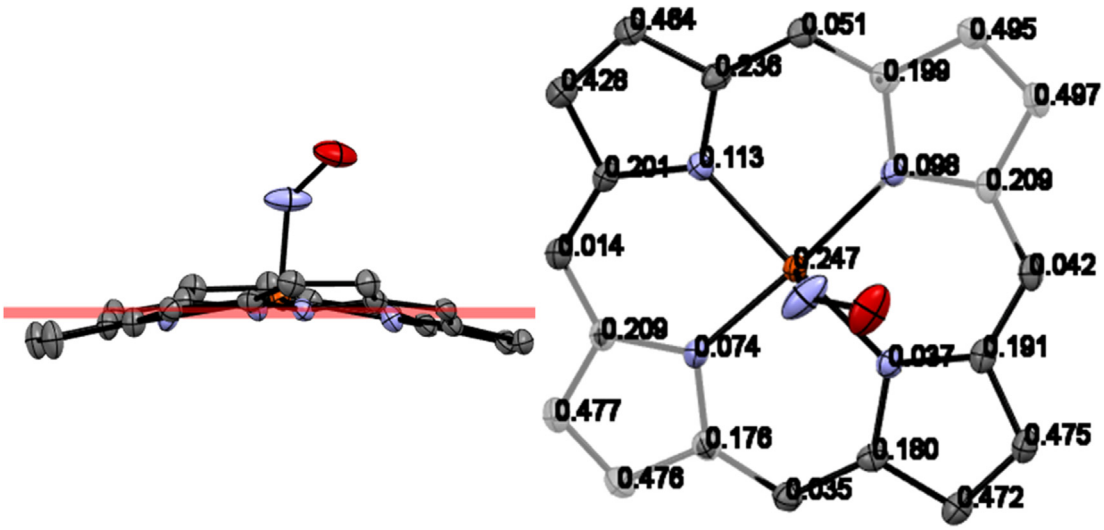

Figure 4. ORTEP plots of the porphyrin core of $(BTMA)_2Mg[Fe^{II}(TPPS)(NO^{\bullet})]$ at the 50% probability level. Left: Saddled porphyrin conformation and porphyrin mean plane, shown in pink. Right: top view, with individual atomic displacements from the porphyrin mean plane, in angstroms.

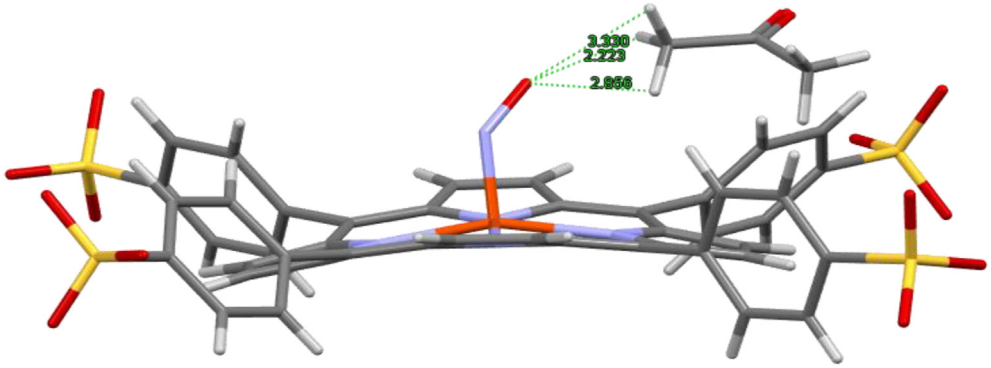

Figure 6. Hydrogen bonding interactions between the NO fragment and a nearby acetone molecule.

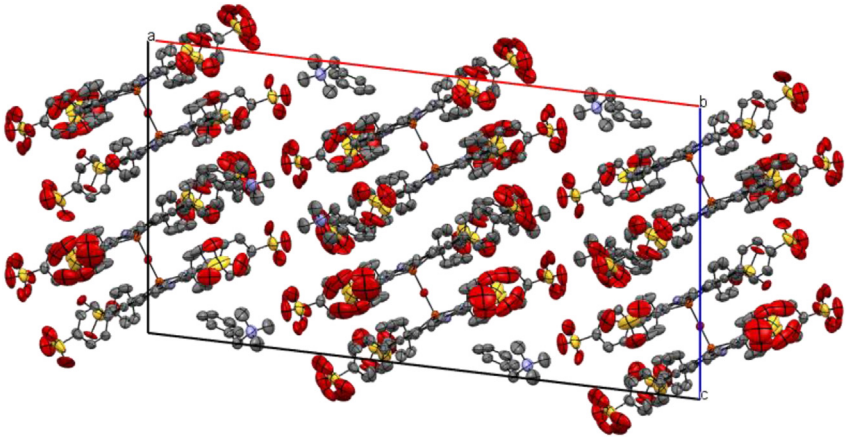

Figure 7. ORTEP plot of $(BTMA)_8[\mu\text{-O-}(Fe^{III}(TPPS))_2]$ at the 50% probability level showing the crystal packing and unit cell. Hydrogen atoms were omitted for clarity.

SQUEEZE algorithm in Olex2, as previously performed with $[Co^{II}(TPPS)]^{3-}$ [8]. The sulfonate groups also show markedly greater disorder than in the nitrosyl complex structure.

As can be seen, dimeric units are close to each other with an interplane separation (IS) of 4.833 Å, which is comparable to the distance between porphyrin planes within the same dimer, indicating the presence of π-π stacking interactions. The Fe-Fe distance between adjacent dimers is 7.77 Å, which is comparable to the value of 7.06 Å found in $[\mu\text{-O-}([Fe^{III}(TMPyP)])_2]^{8+}$. The slip angle (SA) between the dimeric molecules is 52°, again comparable to the value found in $[Fe^{III}(TMPyP)]^{5+}$, which is 57°. Lateral displacements between dimers are also similar: 6.12 Å for $[\mu\text{-O-}([Fe^{III}(TPPS)])_2]^{8-}$ and 5.44 Å for $[\mu\text{-O-}([Fe^{III}(TMPyP)])_2]^{8+}$. These parameters can be visualized in Figure 13 in the Experimental Section.

Figure 8 shows an individual dimer from a lateral (left) and top (right) perspective, where the alternate conformation between the monomers is evident, with dihedral N_{PORF}-Fe-Fe-N_{PORF} angles between 33.6° and 56.3°. This conformation minimizes the steric and electrostatic repulsions between the 4-sulfonatophenyl *meso* substituents. The aromatic rings in the *meso* substituents are perpendicular to the

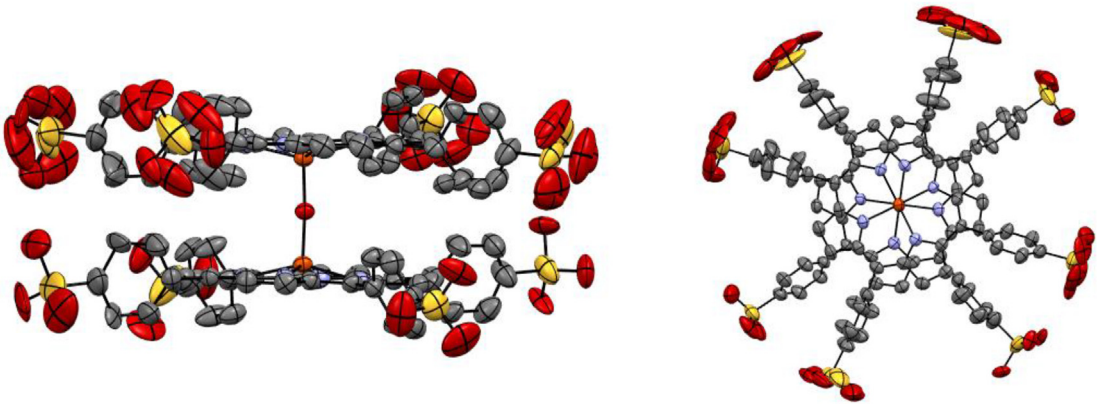

Figure 8. ORTEP plot of $(BTMA)_8[\mu\text{-O-}(Fe^{III}(TPPS))_2]$ at the 50% probability level showing the lateral (left) and top (right) view of an individual dimer molecule. Hydrogen atoms were omitted for clarity.

Table 3. Crystallographic information and selected structural parameters for $(BTMA)_8[\mu\text{-O-}([Fe^{III}(TPPS)])_2]$.

$(BTMA)_8[\mu\text{-O-}(Fe^{III}(TPPS))_2]$	
Crystallographic Information	
Space group	C 2/c
Crystal System	Monoclinic
a (Å)	39.5217 (17)
b (Å)	21.2874 (9)
c (Å)	20.8582 (9)
a (°)	90
β (°)	96.8804 (17)
γ (°)	90
R_1	6.19
Selected distances and angles	
Fe-O (Å)	1.757
Δ Fe out of plane (Å)	0.510
Fe-O-Fe (°)	176.35
Fe-Fe (Å)	3.51
Avg. Fe-N_{PORF} (Å)	2.079
N_{PORF}-Fe-Fe-N_{PORF} dihedral (°)	33.6°–56.3°
PORF-PORF(Å)	4.502
IPS (Å)*	4.833
LS (Å)*	6.12
Slip Angle (°)*	52°

* To visualize these parameters, see Figure 13 in the Experimental section.

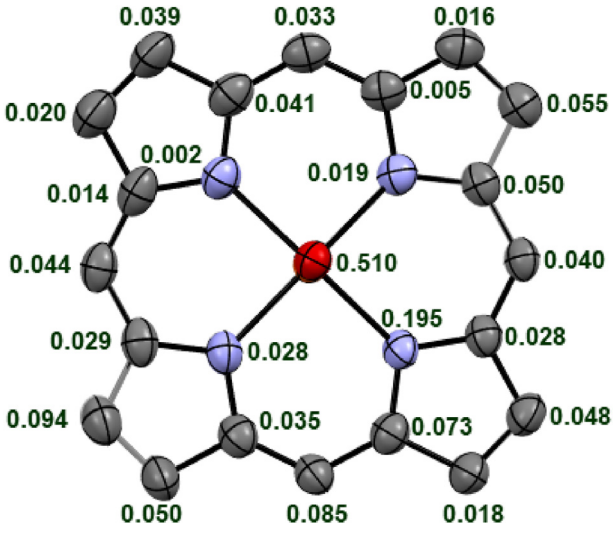

Figure 9. ORTEP plot of $(BTMA)_8[\mu\text{-O-}(Fe^{III}(TPPS))_2]$ at the 50% probability level showing the atomic displacements from the porphyrin mean plane, in angstroms.

porphyrin mean planes, which are parallel within and between dimers. Crystallographic information and relevant structural parameters are shown in Table 3.

The individual displacements (in angstroms) of each atom from the 24-atom porphyrin mean plane are shown in Figure 9. Although the iron atom is considerably displaced from this plane, in this case the porphyrin ring is essentially planar, with no evident saddled or ruffled distortion. This feature possibly maximizes π-π stacking interactions between and within dimers.

Most structural parameters obtained for $[\mu\text{-O-}([Fe^{III}(TPPS)])_2]^{8-}$ are similar to those previously observed for the cationic oxodimeric species $[\mu\text{-O-}([Fe^{III}(TMPyP)])_2](ClO_4)_8{\bullet}4H_2O$ [10]. For example, Fe-O distances (1.757 Å for $[\mu\text{-O-}([Fe^{III}(TPPS)])_2]^{8-}$ and 1.750 Å for $[\mu\text{-O-}([Fe^{III}(TMPyP)])_2]^{8+}$), the Fe-O-Fe angle which remains essentially straight (176.35° and 175.1° respectively), and the average Fe-N_{PORF} distances (2.076 Å and 2.081 Å respectively). The distance between both porphyrin rings within a dimer is also similar, being 4.50 Å in $[\mu\text{-O-}([Fe^{III}(TPPS)])_2]^{8-}$ and 4.43 Å in $[\mu\text{-O-}([Fe^{III}(TMPyP)])_2]^{8+}$.

3. Conclusions and perspectives

The recently reported isolation method for $Na_4[Fe^{II}(TPPS)(NO^{\bullet})]$ [14], along with ion-exchange methods, allowed for the resolution of the crystal structure of the first water-soluble porphyrin nitrosyl complex. Crystalline samples could only be obtained after a counterion exchange procedure, followed by slow acetone vapour diffusion in water, in the absence of oxygen. Additionally, single crystal X-ray diffraction measurements could only be performed at 100K, with crystals collapsing at higher temperatures. In general, the most characteristic structural parameters agree with reported values for nitrosyl porphyrin complexes soluble in organic media. No water molecules are found near the Fe-N-O site, although hydrogen bonding interactions with an acetone molecule can be inferred. The NO ligand is disordered, as is usually the case for these complexes. In general, no significant differences are found in the structural parameters of the water-soluble nitrosyl complexes, compared to their organosoluble analogues. However, as already discussed in previous works, there seems to be an increased difficulty in the crystallization of the complexes from aqueous solutions.

The counterion exchange procedure also allowed us to attempt the structure solving of the ferric precursor $[Fe^{III}(TPPS)]^{3-}$. Fortunately, crystalline samples could also be prepared, although only containing the oxo dimeric form, $[\mu\text{-O-}([Fe^{III}(TPPS)])_2]^{8-}$. The observed structural parameters are in good agreement with those reported for the related cationic complex $[\mu\text{-O-}([Fe^{III}(TMPyP)])_2]^{8+}$.

4. Experimental section

4.1. Preparation of $(BTMA)_3[Fe^{III}(TPPS)]$

$Na_3[Fe^{III}(TPPS)]$ was prepared from $Na_4[H_2(TPPS)]$ available from Frontier Scientific according to literature methods [14]. The sodium counterions were exchanged for benzyltrimethylammonium ($BTMA^+$, Figure 10) cations by obtaining $H_3[Fe^{III}(TPPS)]$ after elution in a protonated DOWEX ion-exchange resin and re-neutralizing with (BTMA)OH. The BTMA hydroxide was prepared by stirring excess Ag_2O with (BTMA)Br in the dark for over 24h until no bromide traces were found in the supernatant, as detected via AgBr precipitation following acidic $AgNO_3$ addition.

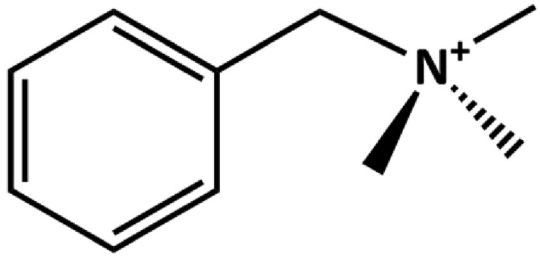

Figure 10. Benzyltrimethylammonium cation ($BTMA^+$).

Figure 11. Crystallization setup for $(BTMA)_2Mg[Fe^{II}(TPPS)\ (NO^{\bullet})]$ under argon. Initially, a deoxygenated aqueous saturated solution of the complex is placed in the vials. Degassed acetone (approximately 10–15 ml) is placed inside the Schlenk tube, surrounding the vials. Needles are punctured through the vials' septa to allow slow vapor diffusion.

4.1.1. Crystallization method

5–8 mg fractions were dissolved in approximately 100 μL methanol to give a saturated solution. The solution was placed into a 2 mL vial and sealed with a new septum. The vial was placed inside a bigger flask containing acetone. A needle was punctured through the septum, and the flask was sealed. Acetone vapour was then allowed to slowly diffuse over the aqueous solution in the dark at 24 °C. Needle-like crystals were collected and measured after several weeks.

4.2. Preparation of $(BTMA)_4[Fe^{II}(TPPS)\ (NO^{\bullet})]$

$(BTMA)_4[Fe^{II}(TPPS)\ (NO^{\bullet})]$ was prepared and isolated from $(BTMA)_3[Fe^{III}(TPPS)]$ following literature procedures reported for $Na_4[Fe^{II}(TPPS)\ (NO^{\bullet})]$ [14], but using (BTMA)OH instead of NaOH during the nitrosylation reaction. The reaction was carried out under strict anaerobic conditions using deoxygenated solvents and reagents. The resulting complex is soluble in water and methanol.

4.2.1. Crystallization method

5–8 mg fractions were separated for crystallization inside a nitrogen glovebox. They were afterwards dissolved in approximately 100 μL of degassed milli-Q water and placed in a 5 mL vial inside an argon-filled Schlenk flask using a Schlenk line. The vial was sealed with a new septum, and 10–15 mLacetone, previously degassed by argon bubbling and 3 freeze-pump-thaw cycles, were placed inside the Schlenk flask. Finally, a needle was punctured through the septum allowing for slow acetone vapor diffusion into the aqueous solution. The system was left under argon at 24 °C in the dark. Thin needle-like crystals were collected after several weeks. The crystallization setup can be seen in Figure 11.

4.3. Single crystal X-ray diffraction measurements

Crystals were first observed using a Nikon polarizing microscope. Suitable samples were measured in a Bruker D8 QUEST ECO diffractometer equipped with a Mo (λ = 0.71073 Å) source, a graphite monochromator and a PHOTON 50™ CMOS detector. All measurements were performed at 100 K using an Oxford Cryosystems *Cryostream 800* device. Data processing was performed using the Apex3 software, and multi-scan corrections were applied. SHELXT direct methods were used in structure resolution and refining steps. Least square fittings based on F2 were performed with SHELXL using Olex2 1.3 software. Mercury software was used for structure visualization and figure selection.

4.3.1. X-ray structural analysis of $BTMA_2Mg[Fe^{II}(TPPS)\ (NO^{\bullet})]$

Crystal data: $C_{44}\ H_{24}\ Fe\ N_5\ O_{13}\ S_4,\ Mg(H_2O)_6,\ 2(C_{10}H_{16}N),\ 4(H_2O),\ 2(C_3H_6O)$. Metallic dark violet, prism. 0.6 × 0.2 × 0.15 mm^3, triclinic, P-1, a = 9.1095(4) Å, b = 19.7734(9) Å, c = 22.9644(10) Å; α= 79.838 (2)°, β = 80.129(2)°, γ = 85.701(2) from 20 degrees of data; T = 99.99K; V = 4007.1(3)$Å^3$, Z = 2; Fw = 1635.87; D_C = 1.356 gcm^{-3}; μ = 0.379 mm^{-1}. **Data collection and processing:** Bruker D8 Quest ECO diffractometer, PHOTON 50™ CMOS, APEX-III detector, Mo Kα (λ = 0.71073 Å), graphite monochromator; $-10 \le h \le 10$, $-23 \le k \le 23$, $-27 \le l \le 27$, 425573 reflections collected, 14391 independent reflections (R_{INT} = 0.1453). **Solution and refinement:** The structure was solved by direct methods with SHELXT. Full-matrix least-squares refinement based on F^2 with SHELXL; 1198 parameters with 374 restraints, final R_1 = 0.0614 (based on F^2) for data with I > 2 σ (I) and R_1 = 0.0875 on 14391 reflections, goodness-of-fit on F^2 = 1.087, largest electron density peak = 1.450 e $Å^{-3}$.

4.3.2. X-ray structural analysis of $(BTMA)_8[\mu\text{-}O\text{-}(Fe^{III}(TPPS))_2]$

Crystal data: $C_{88}\ H_{46}\ Fe_2\ N_8\ O_{24}\ S8 + 2\ (C_{10}H_{16}N) + 6\ (C_{10}H_{16}N)$. These six $BTMA^+$ molecules were modelled using the solvent mask detailed in the BYPASS paper [25]. Metallic dark violet, prism. 0.4 × 0.2 × 0.1 mm^3, monoclinic, C 1 2/c 1a = 39.5217(17) Å, b = 21.2874(9) Å, c = 20.8582 (9) Å; β = 96.8804 (17) ° from 20 degrees of data; T = 99.99K; V = 17421.9(13)$Å^3$, Z = 4; Fw = 2286; D_C = 0.872 gcm^{-3}; μ = 0.311 mm^{-1}. **Data collection and processing:** Bruker D8 Quest ECO diffractometer, PHOTON 50™ CMOS, APEX-III detector, Mo Kα (λ = 0.71073 Å), graphite monochromator; $-47 \le h \le 46$, $-25 \le k \le 25$, $-24 \le l \le 24$,150049reflections collected, 15564independent reflections (R_{INT} = 0.0652). For data collection, cell refinement and data reduction Apex3 software was used. Absorption correction was made by multi-scan. **Solution and refinement:** The structure was solved by direct methods with SHELXT. Full-matrix least-squares refinement based on F^2 with SHELXL; 893 parameters with 114 restraints, final R_1 = 0.0619 (based on F^2) for data with I > 2 σ (I) and R_1 = 0.0850on 15564 reflections, goodness-of-fit on F^2 = 1.066, largest electron density peak = 0.433 e $Å^{-3}$.

In this case, a solvent mask had to be applied using the *SQUEEZE* algorithm in Olex2, as previously performed with $[Co^{II}(TPPS)]^{3-}$ [8]. In this case, 1898 electrons were found in a volume of 8301 $Å^3$ in 1 void per unit cell. This is consistent with the presence of 3 $[C_{10}NH_{16}]$ per asymmetric unit which account for 1992 electrons per unit cell.

4.4. Visualization of structural parameters

4.4.1. $(BTMA)_2Mg[Fe^{II}(TPPS)\ (NO^{\bullet})]$

A schematic representation of some relevant structural parameters of $(BTMA)_2Mg[Fe^{II}(TPPS)\ (NO^{\bullet})]$ can be found in Figure 12.

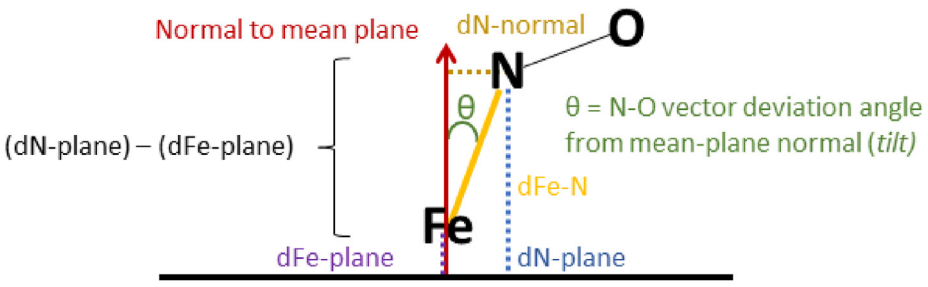

$$\cos(\theta) = \frac{\text{opposite}}{\text{hypotenuse}} = \frac{(\text{dN}-\text{plane}) - (\text{dFe}-\text{plane})}{\text{dFe}-\text{N}}$$

$$\text{dN-normal} = \sin(\theta)*\text{hypotenuse} = \sin(\theta)*\text{dFe-N}$$

Figure 12. Visualization of calculated structural parameters of $(BTMA)_2Mg[Fe^{II}(TPPS)(NO^{\bullet})]$.

4.4.2. $(BTMA)_8[\mu\text{-}O\text{-}(Fe^{III}(TPPS))_2]$

A schematic representation of some relevant structural parameters of $(BTMA)_8[\mu\text{-}O\text{-}(Fe^{III}(TPPS))_2]$ can be found in Figure 13.

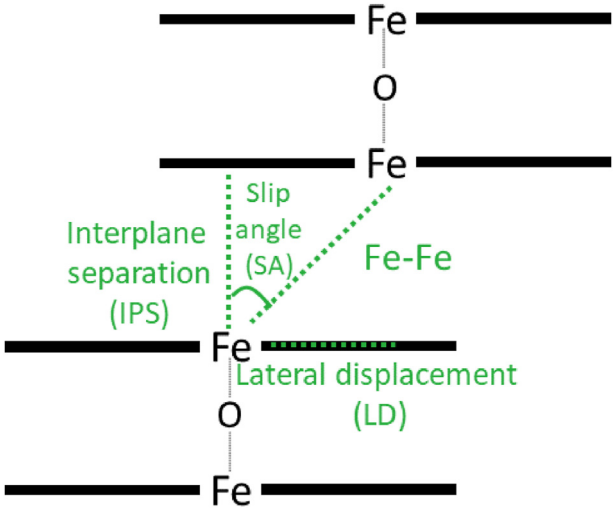

Figure 13. Visualization of characteristic structural parameters found in oxo-dimeric porhyrin species.

Declaration

Author contribution statement

Agostina Mazzeo: Conceived and designed the experiments; Performed the experiments; Wrote the paper.

Carina Gaviglio: Conceived and designed the experiments; Performed the experiments; Analyzed and interpreted the data.

Juan Pellegrino: Conceived and designed the experiments.

Fabio Doctorovich: Conceived and designed the experiments; Contributed reagents, materials, analysis tools or data.

Funding statement

This work was funded and supported by CONICET, Secretaria de Ciencia y Tecnica, Universidad de Buenos Aires (20020170100595BA) and Ministerio de Ciencia, Tecnología e Innovación Productiva (PICT-2015-3854 and PICT-2017-1930).

Data availability statement

Data included in article/supplementary material/referenced in article.

Declaration of interests statement

The authors declare no conflict of interest.

Additional information

Supplementary content related to this article has been published online at https://doi.org/10.1016/j.heliyon.2022.e09555.

References

[1] M.P. Byrn, C.J. Curtis, S.I. Khan, P.A. Sawin, R. Tsurumi, C.E. Strouse, Tetraarylporphyrin sponges. Composition, structural systematics, and applications of a large class of programmable lattice clathrates, J. Am. Chem. Soc. 112 (5) (1990) 1865–1874.

[2] N. Lehnert, E. Kim, H.T. Dong, J.B. Harland, A.P. Hunt, E.C. Manickas, K.M. Oakley, J. Pham, G.C. Reed, V.S. Alfaro, The biologically relevant coordination chemistry of iron and nitric oxide: electronic structure and reactivity, Chem. Rev. 121 (24) (2021) 14682–14905.

[3] J.H. Enemark, R.D. Feltham, Principles of structure, bonding, and reactivity for metal nitrosyl complexes, Coord. Chem. Rev. 13 (4) (1974) 339–406.

[4] G.R.A. Wyllie, W.R. Scheidt, Solid-state structures of metalloporphyrin NOx compounds, Chem. Rev. 102 (4) (2002) 1067–1090.

[5] N. Kundakarla, S. Lindeman, Md.H. Rahman, M.D. Ryan, X-ray structure and properties of the ferrous octaethylporphyrin nitroxyl complex, Inorg. Chem. 55 (5) (2016) 2070–2075.

[6] B. Hu, J. Li, One electron makes differences: from heme $FeNO^7$ to $FeNO^8$, Angew. Chem. Int. Ed. 54 (36) (2015) 10579–10582.

[7] N. Lehnert, H.T. Dong, J.B. Harland, A.P. Hunt, C.J. White, Reversing nitrogen fixation, Nat. Rev. Chem 2 (10) (2018) 278–289.

[8] S. Mathura, A.S. de Sousa, M.A. Fernandes, H.M. Marques, 5,10,15,20-Tetra-p-Phenylsulfonyporphinatocobalt(III), a water-soluble Co(III) porphyrin, Inorg. Chim. Acta. 392 (2012) 108–111.

[9] H. Kanemitsu, R. Harada, S. Ogo, A water-soluble iridium(III) porphyrin, Chem. Commun. 46 (18) (2010) 3083–3085.

[10] M.A. Ivanca, A. Graham Lappin, W. Robert Scheidt, Water-soluble ferric porphyrinates: solution and solid-state species, Inorg. Chem. 30 (4) (1991) 711–718.

[11] F.C.F. Körber, J.R.L. Smith, S. Prince, P. Rizkallah, C.D. Reynolds, D.R. Shawcross, Crystal structure of monomeric hydrated iron(III) 5,10,15,20-tetra(N-Methyl-4-Pyridinio)Porphyrin pentachloride; an ionic Haem model, J. Chem. Soc., Dalton Trans. 12 (1991) 3291–3294.

[12] H. Seki, M. Hoshino, S. Kounose, Reduction of a water-soluble iron(III) porphyrin and an iron(II) nitrosyl porphyrin by benzophenone ketyl radical, J. Chem. Soc., Faraday Trans. 92 (14) (1996) 2579–2583.
[13] P.C. Ford, B.O. Fernandez, M.D. Lim, Mechanisms of reductive nitrosylation in iron and copper models relevant to biological systems, Chem. Rev. 105 (6) (2005) 2439–2455.
[14] A. Mazzeo, J. Pellegrino, F. Doctorovich, Water-soluble nitroxyl porphyrin complexes FeIITPPSHNO and FeIITPPSNO– obtained from isolated FeIITPPSNO, J. Am. Chem. Soc. 141 (46) (2019) 18521–18530.
[15] L.E. Goodrich, F. Paulat, V.K.K. Praneeth, N. Lehnert, Electronic structure of heme-nitrosyls and its significance for nitric oxide reactivity, sensing, transport, and toxicity in biological systems, Inorg. Chem. 49 (14) (2010) 6293–6316.
[16] W.R. Scheidt, Y.J. Lee, Recent advances in the stereochemistry of metallotetrapyrroles, in: J.W. Buchler (Ed.), Metal Complexes with Tetrapyrrole Ligands I, Structure and Bonding, Springer, Berlin, Heidelberg, 1987, pp. 1–70.
[17] J.A. Shelnutt, X.-Z. Song, J.-G. Ma, S.-L. Jia, W. Jentzen, C.J. Medforth, C.J. Medforth, Nonplanar porphyrins and their significance in proteins, Chem. Soc. Rev. 27 (1) (1998) 31–42.
[18] W.R. Scheidt, H.F. Duval, T.J. Neal, M.K. Ellison, Intrinsic structural distortions in five-coordinate (Nitrosyl)Iron(II) porphyrinate derivatives, J. Am. Chem. Soc. 122 (19) (2000) 4651–4659.
[19] J. Bhuyan, S. Sarkar, Nitrous-acid-mediated synthesis of iron–nitrosyl–porphyrin: PH-dependent release of nitric oxide, Chem. Asian J. 7 (11) (2012) 2690–2695.
[20] L.E. Goodrich, S. Roy, E.E. Alp, J. Zhao, M.Y. Hu, N. Lehnert, Electronic structure and biologically relevant reactivity of low-spin {FeNO}8 porphyrin model complexes: new insight from a bis-picket fence porphyrin, Inorg. Chem. 52 (13) (2013) 7766–7780.
[21] N.J. Silvernail, M.M. Olmstead, B.C. Noll, W.R. Scheidt, Tetragonal to triclinic—a phase change for [Fe(TPP)(NO)], Inorg. Chem. 48 (3) (2009) 971–977.
[22] G.R.A. Wyllie, N.J. Silvernail, A.G. Oliver, C.E. Schulz, W.R. Scheidt, Iron nitrosyl "natural" porphyrinates: does the porphyrin matter? Inorg. Chem. 53 (7) (2014) 3763–3768.
[23] P. Böhm, H. Gröger, Iron(III)-Porphyrin complex FeTSPP: a versatile water-soluble catalyst for oxidations in organic syntheses, biorenewables degradation and environmental applications, ChemCatChem 7 (1) (2015) 22–28.
[24] L.E. Laverman, P.C. Ford, Mechanistic studies of nitric oxide reactions with water soluble iron(II), cobalt(II), and iron(III) porphyrin complexes in aqueous solutions: implications for biological activity, J. Am. Chem. Soc. 123 (47) (2001) 11614–11622.
[25] P. van der Sluis, A.L. Spek, BYPASS: an effective method for the refinement of crystal structures containing disordered solvent regions, Acta Crystallogr. A 46 (3) (1990) 194–201.